Carbon Nanotubes by a CVD Method. Part I: Synthesis and Characterization of the (Mg, Fe)O Catalysts

Pierre Coquay,[†] Eddy De Grave,[†] Alain Peigney,[‡] Robert E. Vandenberghe,[†] and Christophe Laurent*[,‡]

NUMAT, Department of Subatomic and Radiation Physics, University of Ghent, Proeftuinstraat 86, B-9000 Gent, Belgium, and CIRIMAT, UMR CNRS 5085/LCMIE, Centre Interuniversitaire de Recherche et d'Ingénierie des Matériaux, Université Paul-Sabatier, 31062 Toulouse Cedex 4, France

The controlled synthesis of carbon nanotubes by chemical vapor deposition requires tailored and well-characterized catalyst materials. We attempted to synthesize $Mg_{1-x}Fe_xO$ oxide solid solutions by the combustion route, with the aim of performing a detailed investigation of the influence of the synthesis conditions (nitrate/urea ratio and the iron content) on the valency and distribution of the iron ions and phases. Notably, characterization of the catalyst materials is performed using ^{57}Fe Mössbauer spectroscopy, X-ray diffraction, and electron microscopy. Several iron species are detected including Fe^{2+} ions substituting for Mg^{2+} in the MgO lattice, Fe^{3+} ions dispersed in the octahedral sites of MgO, different clusters of Fe^{3+} ions, and $MgFe_2O_4$-like nanoparticles. The dispersion of these species and the microstructure of the oxides are discussed. Powders markedly different from one another that may serve as model systems for further study are identified. The formation of carbon nanotubes upon reduction in a H_2/CH_4 gas atmosphere of the selected powders is reported in a companion paper.

Introduction

Catalytic chemical vapor deposition (CCVD) is widely used for the synthesis of carbon nanotubes (CNTs). This method, similar to those used for several decades for the synthesis of various filamentous forms of carbon, involves the catalytic decomposition of hydrocarbons or carbon monoxide on transition-metal nanometric particles. Theoretical and experimental results[1−4] show that CNTs are produced by catalyst particles below ca. 3 nm in diameter. One of the key points is to tailor the starting material so that the catalyst particles retain a small size and indeed are active for CNT formation under given experimental conditions (nature of carbon source, temperature, etc). However, relatively few articles report detailed studies on the starting material.[5−7] We have proposed an original CCVD method,[8] showing that the reduction of α-$Al_{1.9}Fe_{0.1}O_3$ in a H_2/CH_4 atmosphere produces pristine Fe nanoparticles at a temperature high enough for them to catalyze the decomposition of CH_4 and for the in-situ formation of CNTs including single-walled CNTs (SWNTs). Characteristics of the starting alumina-based oxide such as the iron content,[9] the crystallographic form,[10] and the specific surface area[11] have been investigated with the aim of increasing the proportion of single-walled CNTs (SWNTs). Using $Mg_{1-x}M_xAl_2O_4$-based solid solutions, the composition of the starting oxide and thus the composition of the in situ-formed catalytic particles were also investigated for M = Fe, Co, and Ni[12,13] and M = Fe/Co, Fe/Ni, and Co/Ni.[14,15]

$Mg_{1-x}Co_xO$ powders were also studied and are notably interesting because a simple soaking in HCl allows us to separate the CNTs from the CNT−Co−MgO powders formed upon reduction in H_2/CH_4.[2,3] However, undesirable Co_3O_4 particles, leading to thick carbon nanofibers rather than to CNTs, may also be formed during the synthesis of the oxide using the combustion route.[16,17] This method involves the exothermic redox reaction between a mixture of metal nitrates (oxidizer) and urea (fuel). The so-called stoichiometric composition of the redox mixture is usually calculated using the total oxidizing and reducing valencies of the metal nitrates and urea, which serve as numerical coefficients for the stoichiometric balance, so that the equivalency ratio is equal to unity.[18] However, these calculations are made using several hypotheses. One is that the oxidizing power of the oxygen in the reaction atmosphere (air) is not taken into account. Another is that N_2 is the only nitrogen-containing product of the reaction so that zero is taken as the valency for nitrogen. In fact, ammonia and nitrogen oxides are also released, and thus the actual valency to be used is not precisely known. Zhang and Stangle[19] have proposed that there is a range of ratios defining a stoichiometric region for which the desired product may be prepared, whereas lower ratios are too oxidizing and higher ratios, too reducing. It was indeed shown[20] that by varying the urea/nitrate ratio the formation of Co_3O_4 particles was avoided. However, more details on the valency and the precise distribution of the cobalt ions in the MgO-based powders were not known. Thus, we attempt in the present study to synthesize $Mg_{1-x}Fe_xO$ oxide solid solutions and to characterize them using ^{57}Fe Mössbauer spectroscopy. The aim of this work is to study the influence of both the urea/nitrate ratio (also called the urea ratio) and the iron content on the valency and distribution of the iron ions and phases. The formation of CNTs by reduction in a H_2/CH_4 atmosphere of selected specimens is reported in a companion paper.[21]

Experimental Section

Synthesis. The appropriate amounts of magnesium and iron nitrates were mixed with the desired quantity of urea (NH_2−

† University of Ghent.
‡ Université Paul-Sabatier.

$CO-NH_2$) to produce 2 g of a $Mg_{1-x}Fe_xO$ solid solution (x = 0.025; 0.05, 0.075; 0.10; 0.15; 0.20; 0.40). To increase the substitution ratio of the iron cations in the MgO lattice, the urea proportion was multiplied by 2 to 8 times the value calculated for the so-called stoichiometric ratio. It was thus expected to determine the stoichiometric region.[19] The reagents were mixed with 3.3 mL of water. The dissolution of the reagents is endothermic and leads to an increase of the salt weights. The mixture had to be continuously stirred and slightly warmed to get a clear, homogeneous solution. The dissolution time increased with increasing urea ratio, reaching 20 to 30 min for a urea ratio of 8. After total dissolution, the dish containing the solution had to be rapidly introduced into the furnace; otherwise, a red precipitate formed at the bottom. With a urea ratio of 8, the solution completely froze after a few seconds. However, in all cases, rewarming the mixture led back to total dissolution. The Pyrex dish containing the clear, homogeneous solution was placed in a furnace preheated to 600 °C. The solution immediately started to boil and dehydrate. Then, the combustion process itself took place, as described in a later section. The combustion product was slightly manually ground to produce a powder.

For the sake of brevity, the Fe/MgO oxide powders will be referred to according to the following example: Fe10U4 will be used for a supposed $Mg_{0.90}Fe_{0.10}O$ solid solution prepared with a urea ratio of 4 (i.e., 4 times the so-called stoichiometric ratio).

Characterization. Elemental analysis of carbon and nitrogen was performed by flash combustion with an accuracy of ±2%. Specific surface-area measurements were performed using N_2 adsorption at liquid N_2 temperature in a Micromeritics Flow Sorb II 2300 apparatus (BET method). This instrument gives a specific surface-area value from one point (i.e., one adsorbate pressure) and requires calibration. The reproducibility of the results was determined to be in the ±3% range.

X-ray diffraction (XRD) patterns were recorded with a Siemens D501 diffractometer using Cu Kα radiation and were computer analyzed with the GUFI 5.0 program.[22e] For lattice-parameter measurements, the powders were mixed with NaCl as an internal standard, and the calculations were performed with the UnitCell program.[23] The crystallite sizes were evaluated from the widths at half-maximum of the diffraction peaks using the well-known Scherrer formula, with an accuracy on the order of 20%.

Mössbauer spectra (MS) were recorded with a ^{57}Co (Rh) source using a conventional time-mode spectrometer with a constant-acceleration drive and a triangular reference signal. Accumulation of the data was performed in 1024 channels until a background of at least 10^6 counts per channel was reached. The spectrometer was calibrated by collecting at room temperature (RT) the MS of a standard α-Fe foil, and the isomer-shift values quoted hereafter are with reference to this standard. The measured absorbers were prepared with an amount of powder corresponding to 10 mg of iron atoms per square centimeter. Measurements between 14 K and RT were performed by mounting the sample in a closed-cycle refrigerator. The spectra were generally analyzed assuming symmetrical components with Lorentzian line shapes. Asymmetrical Mössbauer patterns were fitted with a model-independent hyperfine-field or quadrupole-splitting distribution with Lorentzian-shaped elemental spectra.[24] The quoted isomer-shift and quadrupole-shift values are in that case average values for the distributed parameters. However, the environment fluctuations of the Mössbauer atom responsible of the distribution of a hyperfine parameter have generally some influence on the other parameters. In most cases, good results are obtained by considering a linear correlation between the different distributions. The following linear correlation between the isomer shift (δ) and/or quadrupole shift ($2\epsilon_Q$) and the hyperfine field (H_{hf}) of a distributed sextet can be used: $\delta_k = \delta_0 + D_\delta(H_{hf,max} - H_{hf,k})$ and $2\epsilon_{Q,k} = 2\epsilon_{Q,0} + D_\epsilon(H_{hf,max} - H_{hf,k})$ where δ_0 and $2\epsilon_{Q,0}$ are the isomer-shift and quadrupole-shift values correponding to $H_{hf,max}$. Similarly, in the case of a distributed doublet, the following linear correlation between the isomer shift (δ) and quadrupole splitting (ΔE_Q) can be used: $\delta_k = \delta_0 + D_\delta(\Delta E_{Q,max} - \Delta E_{Q,k})$ where δ_0 is the isomer-shift value correponding to $\Delta E_{Q,max}$.

The oxide powders were observed with a JEOL JSM 6400 scanning electron microscope (SEM) and with a JEOL 2010 transmission electron microscope (TEM). A Tracor Voyager energy-dispersive X-ray (EDX) analyzer (Ge detector) able to work with a probe size as small as 4 nm was used for quantitative analyses of very small areas.

Results and Discussion

Combustion Process. The nitrate−urea solution that was placed in a furnace preheated to 600 °C immediately started to boil and dehydrate. The decomposition of the reagents was accompanied by a large release of gases (nitrogen oxides and ammonia), increasing in proportion to the urea content. The resulting paste then frothed and formed a foam that swelled in proportion to the gas release. For a urea ratio of 1, a thin layer was formed at the bottom of the dish, whereas for a urea ratio of 4, the full dish was filled by the foam. For a ratio of 8, part of the foam even expanded over the rim of the dish. Once the gas release was complete, the foam blazed, and a white flame appeared over the full dish. In most cases, the reaction was so violent that the flame spread outside the oven, the door of which was left open during the process. The violence of the reaction increased with the urea ratio, reaching a maximum for urea ratios between 3 and 5. The temperature of the oven then went up to 700 °C, and the local temperature at the flame was evaluated to be 1200 °C. However, for higher ratios, the intensity of the flame decreased, and the reaction was less violent. For a urea ratio of 8, there was no blazing but just a glimmer appearing at one point of the foam and slowly spreading over the foam. In this case, the temperature of the oven did not exceed 600 °C. The local flame temperature could not be evaluated, but it is clear that the thermal conditions of the combustion process were very different from those obtained with lower urea ratios. The total combustion process was longer with increasing urea ratios, from 5 min for low ratios to 10 min for a ratio of 8. This is mainly due to the increasing gas release at the start of the process.

Up to a urea ratio of 3, the product that came out of the oven appeared to be a dark-red crust stuck at the bottom of the dish. For higher urea ratios, the product had a somewhat solid consistency and could be taken out of the dish in one piece. Its volume was comparable to the global volume obtained after the gas release during the combustion process. All of the products appeared to be homogeneous but with a color varying from dark red for a urea ratio of 1 to greenish for a ratio of 4 and back to light red for a ratio of 8. It is interesting that red is commonly associated with Fe^{3+} ions and green usually corresponds to Fe^{2+} ions.

For practical reasons, we also attempted to produce batches of 6 g of oxide at a time, the size of the dish being fixed at 900 mL by the size of the oven. For a urea ratio of 1, no difference was observed compared to the 2-g preparation, and the same

TABLE 1: Specific Surface Area S_{ss} of the Fe/MgO Oxide Powders Synthesized by Combustion[a]

urea ratio	cat. % iron	oxide	S_{ss} (m^2/g)
1	5	Fe5U1	13.4 ± 3.1
	7.5	Fe7.5U1	22.1 ± 1.0
	10	Fe10U1	27.1 ± 4.4
	15	Fe15U1	30.6 ± 1.4
	20	Fe20U1	29.7 ± 2.7
2	10	Fe10U2	25.0 ± 4.1
3	10	Fe10U3	9.0 ± 0.3[b]
3.5	10	Fe10U3.5	5.3 ± 0.2
3.75	5	Fe5U3.75	8.0 ± 0.3[b]
	10	Fe10U3.75	5.6 ± 0.2[b]
4	5	Fe5U4	6.8 ± 0.8
	10	Fe10U4	5.7 ± 1.0
4.25	5	Fe5U4.25	7.1 ± 0.2[b]
	10	Fe10U4.25	5.0 ± 0.2[b]
4.5	10	Fe10U4.5	6.5 ± 0.2
5	10	Fe10U5	19.2 ± 0.6[b]
6	10	Fe10U6	43.6 ± 1.3[b]
8	5	Fe5U8	43.5 ± 2.1
	10	Fe10U8	49.0 ± 4.5
	15	Fe15U8	50.1 ± 1.5
	20	Fe20U8	49.1 ± 8.9

[a] The oven was preheated to 600 °C, and batches were 2 g each. Average values are given for different combustion batches except for those denoted by [b] indicating powders that were synthesized only once. The inaccuracy values are discussed in the text.

dark-red crust appeared at the bottom of the dish after the combustion process. For a urea ratio of 4, the volume expansion of the oxide did not increase considerably compared to the volume of the 2-g preparation, but an inhomogeneous product was obtained: green inside and red outside. This could reveal an inhomogeneous repartitioning of Fe^{2+} and Fe^{3+} ions in the oxide. For a urea ratio of 8, most of the foam overflowed in the oven, and the resulting product contained in the dish after the combustion process was quantitatively and qualitatively comparable to the preparation for 2 g of oxide.

The quantity of 2 g per batch was thus considered to be the optimum choice for comparative studies with powders containing different iron contents (from 2.5 to 40 cat. %). Changing the iron content had little influence on the combustion reaction and on the aspect of the final product as described above. The most noticeable difference is that higher iron contents yielded a more pronounced color (either red or green) in the final product.

Finally, chemical analysis indicates the presence of only traces of carbon and nitrogen on the order of 0.1 wt % in most oxide powders, regardless of the urea ratio used for the combustion. The decomposition of urea can hence be considered to be complete for all combustion processes, and the presence of compounds involving carbon or nitrogen in the resulting oxide powders can be ruled out.

Specific Surface Area. The specific surface area S_{ss} of several powders taken at different places in a same combustion batch are within the instrumental accuracy of ±3%, showing the good homogeneity of the product. In most cases, however, the S_{ss} values of samples of the same oxide taken from different combustion batches are outside this error bar. This is because the combustion is a very fast and violent process that is not fully controlled. When more than 2 g of an oxide was required for further studies, batches containing powders with S_{ss} values within the error bar of ±3% were mixed together. S_{ss} indeed appears to be the most sensitive parameter distinguishing combustion batches for the same composition.

The S_{ss} values (Table 1) are average values with an error range covering all of the measured S_{ss} values representative of the oxide. For the powders that were synthesized only once, the S_{ss} values are reported with an (underestimated) accuracy of ±3%. Figure 1 shows the S_{ss} values for the Fe10 oxides versus the urea ratio used in the preparation. S_{ss} initially decreases with increasing urea ratio and reaches a flat minimum for urea ratios between 3.5 and 4.5. Subsequently, S_{ss} increases to a maximum for a urea ratio of 8. A similar evolution can be extrapolated from the S_{ss} values of the Fe5 oxides (Table 1). Moreover, for a urea ratio of 1, an increase of the iron content in the oxide gives rise to a proportional increase of S_{ss} with saturation for 15 cat. % iron. On the contrary, for urea ratios of 3.75, 4, and 4.25, increasing the iron content in the oxide from 5 to 10 cat. % tends to decrease S_{ss} slightly. For a urea ratio of 8, S_{ss} increases from 5 to 10 cat. % iron and then remains constant for higher iron contents, thus following the same trend as in the case of oxides prepared with a urea ratio of 1 but with a smaller influence of the iron content on S_{ss}.

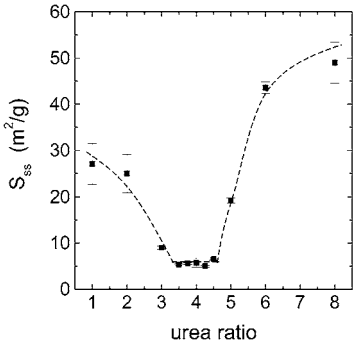

Figure 1. Specific surface area of the Fe10 oxide powders versus the urea ratio used for the combustion. The dashed line is a guide for the eye.

X-ray Diffraction. Figure 2a shows the XRD patterns of Fe10U1, Fe10U4, and Fe10U8 where the five characteristic peaks of MgO are well resolved. A minor phase corresponding to $MgFe_2O_4$ is also detected. An enlargement of the area corresponding to the main peak of $MgFe_2O_4$ (Figure 2b) reveals an intensity minimum of this reflection line for Fe10U4 and a strong increase of the intensity of the MgO(111) peak. Note that the $MgFe_2O_4$ peak is more intense and narrow for Fe10U8. One could propose that the presence of discrete $MgFe_2O_4$ particles of different sizes, but nevertheless relatively small, at the surface of the MgO-based grains for Fe10U1 and Fe10U8 could account for the evolution of S_{ss} as described above. However, this hypothesis will be ruled out, as discussed later, in light of SEM images.

For ideal $Mg_{1-x}Fe_xO$ solid solutions, all iron should be in the divalent state and should substitute for Mg^{2+}. As the ionic radius of Fe^{2+} is larger than the ionic radius of Mg^{2+}, the unit-cell parameter should increase with an increasing iron-substitution ratio following Vegard's law. However, several authors[25−28] have shown that $Mg_{1-x}Fe_xO$ solid solutions present a positive shift from ideality. Figure 3 shows the MgO unit-cell parameter of the Fe10 oxides versus the urea ratio used for the combustion. The unit-cell parameter increases with the urea ratio, reaches a flat maximum for ratios between 3.5 and 4.5, and subsequently decreases for higher ratios so that the unit-cell parameter is equivalent for urea ratios of 1 and 8. Referring to Berthet,[25] the unit-cell parameters of Fe10U1 and Fe10U8 correspond to poorly substituted MgO whereas the unit-cell parameter of Fe10U4 corresponds to a substitution ratio of about 5 cat. %, which is half of the desired value. This is in agreement with the XRD patterns of Figure 2 showing an increased partitioning of the $MgFe_2O_4$ phase for urea ratios of 1 and 8 compared to a

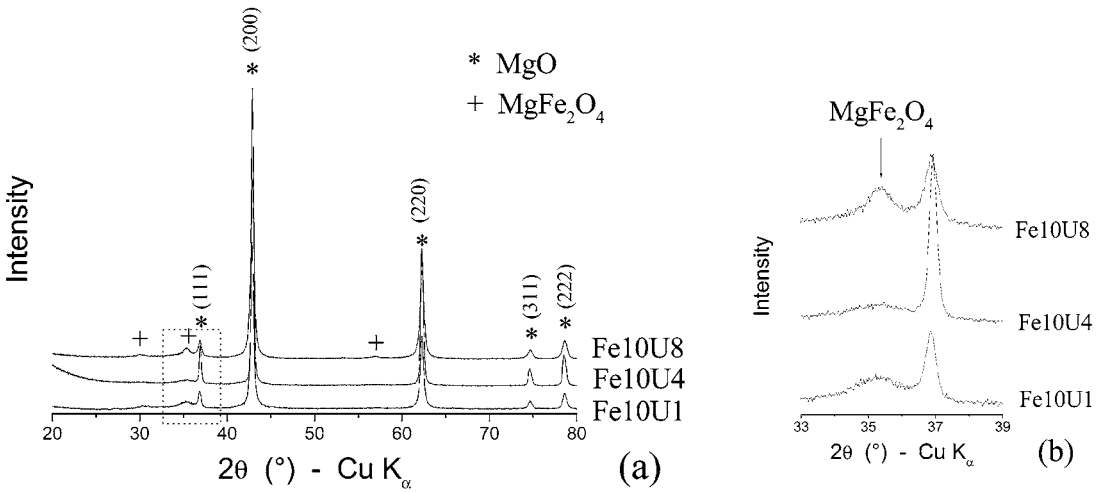

Figure 2. XRD patterns of Fe10U1, Fe10U4, and Fe10U8 (a) and enlargement of the area (cf. dashed square) corresponding to the most intense peak of $MgFe_2O_4$ (b).

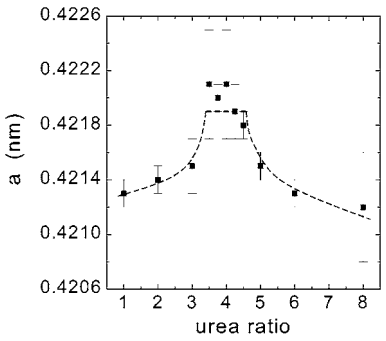

Figure 3. MgO unit-cell parameter *a* of the Fe10 oxide powders versus the urea ratio used for the combustion. The dashed line is a guide for the eye.

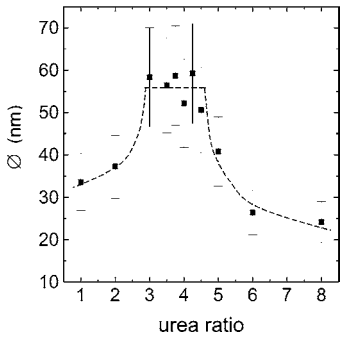

Figure 4. Average MgO crystallite size ∅ of the Fe10 oxide powders versus the urea ratio used for the combustion. The dashed line is a guide for the eye.

urea ratio of 4. It thus appears that urea ratios between 3.5 and 4.5 correspond to the nearest approximation of the desired stoichiometry for the synthesis of Fe/MgO solid solutions prepared according to the considered combustion process.

Figure 4 shows the average MgO crystallite size of the Fe10 oxides versus the urea ratio used for the combustion. Taking into account the large error bars, a flat maximum can be suggested for ratios between 3 and 4.5. As described in the Experimental Section, the increase of the urea ratio from 1 to 4 corresponds to an increase of the reaction temperature, which favors sintering of the material and gives rise to larger crystallites. Moreover, the more violent reaction also leads to an increase of the iron in solution in MgO, as seen in Figure 3. Several authors[29,30] have shown that $Mg_{1-x}Fe_xO$ solid solutions contain some proportion of Fe^{3+} that increases with the amount of iron in solution. These Fe^{3+} ions are associated with vacancies in the MgO lattice, so more iron in solution corresponds to an increase of the vacancy concentration, which favors the diffusion processes during thermal treatments and gives rise to an increase of the crystallite size.[29,31,32] For higher urea ratios, the reaction temperature is lower, and the solubility of iron in MgO decreases, leading to smaller crystallites. Moreover, the higher expansion due to the gas release, notably for a urea ratio of 8, should also lead to smaller MgO crystallites. Indeed, the crystallite size seems to be smaller in Fe10U8 than in Fe10U1, but this cannot be asserted because of the large error bars on these values (Figure 4).

Finally, the average $MgFe_2O_4$ crystallite size could not be determined because of the weak signals in the XRD patterns (Figure 2). However, it appears that the $MgFe_2O_4$ peak is qualitatively broader for Fe10U1 than for Fe10U8 (Figure 2b), revealing smaller $MgFe_2O_4$ particles in the former specimen.

^{57}Fe Mössbauer Spectroscopy. The literature reports numerous Mössbauer studies of iron-substituted MgO prepared by various methods. A relevant fact is that most of the resulting oxide solid solutions involve Fe^{2+} and Fe^{3+} ions. The Fe^{2+} ions substitute for Mg^{2+} on octahedral (O_h) sites and tend to form clusters.[28,31,33−37] The Fe^{3+} ions substitute for Mg^{2+} on O_h sites and are associated with vacancies. Clustering of Fe^{3+} may induce considerable deformation of the fcc lattice of MgO, favoring the transfer of part of the Fe^{3+} ions to tetrahedral (T_d) sites. These clusters can then be considered to be nuclei for spinel formation since the oxygen arrangement is the same in both structures. Many authors have indeed emphasized a narrow association between $Mg_{1-x}Fe_xO$ solid solutions and spinel-structured $MgFe_2O_4$.[34,38−40] A prolonged annealing treatment in air allows for the complete transformation of a $Mg_{1-x}Fe_xO$ solid solution in MgO with total phase partitioning of $MgFe_2O_4$. However, it is difficult to characterize accurately the intermediate steps consisting of more or less agglomerated Fe^{3+} ions in a distorted undefined structure. Principally, the presence of large clusters considered to be $MgFe_2O_4$-like particles can be confirmed by the detection of T_d Fe^{3+}. Moreover, the study of superparamagnetic relaxation at low temperature can produce information on the degree of clustering of the Fe^{3+} ions.

Considering the results of the previous sections, Fe10U1, Fe10U4, and Fe10U8 were selected to be measured between 14 K and RT. The Mössbauer parameters are given in Tables 2, 3, and 4, respectively. Typical MS are presented in Figures 5, 6, and 7, respectively. For the measurements at RT, no

TABLE 2: Mössbauer Parameters of Fe10U1 Measured between 14 K and RT[a]

	(super)para Fe^{3+}					magnetic $MgFe_2O_4$-like						
T(K)	δ	ΔE_Q[c]	D_δ	Γ	P	δ	H_{hf}[d]	$2\epsilon_Q$	D_δ	D_ϵ	Γ	P
14	0.42[b]	0.48		1.07	7.5	0.41	508	0.01	−0.0009	−0.0017	0.49	92.5
30	0.42	0.77		0.63	25.5	0.41	500	0.01	−0.0014	−0.0013	0.44	74.5
		1.43										
50	0.42	0.69	0.0461	0.56	33.5	0.41	491	−0.02	−0.0006	−0.0015	0.46	66.5
	0.39	1.20										
75	0.42	0.65	0.0246	0.51	38.0	0.41	478	0.01	−0.0001	0.0004	0.61	62.0
	0.41	1.10										
100	0.41	0.68	0.0322	0.56	50.5	0.40	460	0.01	0.0002	0.0004	0.53	49.5
	0.39	1.25										
125	0.40	0.67	0.0435	0.61	65.0	0.40[b]	244	0.01[b]			0.90	35.0
	0.37	1.35										
150	0.39	0.57	0.0120	0.57	80.5	0.40[b]	106	0.01[b]			0.32	19.5
	0.38	0.95										
	0.37	1.55										
175	0.37	0.49	0.0108	0.53	88.0	0.40[b]	91	0.01[b]			0.25	12.0
	0.37	0.90										
	0.36	1.80										
220	0.34	0.42	0.0107	0.50	100							
	0.34	0.85										
	0.33	1.55										
RT	0.31	0.37	0.0160	0.41	100							
	0.30	0.80										
	0.29	1.30										
RT	0.30	0.49	−	0.50	60.0							
bis	0.30	0.91		0.43	29.0							
	0.27	1.38		0.43	11.0							

[a] (Super)para: (super)paramagnetic; H_{hf}: hyperfine field at the maximum of the distribution (kOe); δ: (average) isomer shift (mm/s); ΔE_Q: quadrupole splitting at the maxima of the distribution (mm/s); $2\epsilon_Q$: (average) quadrupole shift (mm/s); D_δ: linear correlation coefficient between the isomer shift and quadrupole splitting or hyperfine field; D_ϵ: linear correlation coefficient between the quadrupole shift and hyperfine field; Γ: Lorentzian line width (mm/s); P: proportion (%). [b] Fixed parameter. [c] Quadrupole-splitting distribution from 0.20 to 2.00 mm/s. [d] Hyperfine-field distribution from 60 to 560 kOe.

TABLE 3: Mössbauer Parameters of Fe10U4 Measured between 14 K and RT[a]

	(super)para Fe^{2+}				(super)para Fe^{3+}					magnetic $MgFe_2O_4$-like						
T(K)	δ	ΔE_Q[c]	Γ	P	δ	ΔE_Q[d]	D_δ	Γ	P	δ	H_{hf}[e]	$2\epsilon_Q$	D_δ	D_ϵ	Γ	P
14	1.23	0.45	0.75	30.5	0.47	0.44	-	0.97	13.5	0.41	492	0.02	−0.0003	−0.0005	0.46	56.0
		1.31														
30	1.17	0.45	0.50	38.5	0.46	0.37	−0.0223	0.45	21.0	0.41	489	0.00	−0.0002	−0.0001	0.40	40.5
		1.23			0.47	1.00										
50	1.18	0.40	0.54	41.5	0.46	0.45	−0.0322	0.61	37.5	0.42	488	−0.01	−0.0000	−0.0010	0.24	21.0
		1.16			0.47	1.00										
75	1.15	0.41	0.59	42.0	0.46	0.40	−0.0101	0.49	44.0	0.41	484	0.03	−0.0010	−0.0004	0.27	14.0
		1.12			0.47	0.95										
100	1.14	0.42	0.52	40.0	0.46	0.46	−0.0100	0.55	50.5	0.41[b]	463	0.01[b]			0.22	9.5
		1.15			0.47	0.95										
150	1.10	0.35	0.46	36.5	0.45	0.53	−0.0067	0.62	58.0	0.40[b]	455	0.01[b]			0.21	5.5
		1.00			0.46	1.00										
200	1.08	0.25	0.45	37.0	0.42	0.45	−0.0152	0.54	63.0							
		0.70			0.44	0.93										
250	1.06	0.22	0.48	38.5	0.37	0.48	−0.0503	0.57	61.5							
		0.55			0.41	1.02										
RT	1.04	0.20	0.27	38.0	0.31	0.46	−0.1385	0.53	62.0							
		0.48			0.40	1.10										
RT	1.04	0.20	0.34	37.0	0.32	0.49	−	0.57	36.0							
bis		0.48			0.41	1.12		0.67	27.0							

[a] (Super)para: (super)paramagnetic; H_{hf}: hyperfine field at the maximum of the distribution (kOe); δ: (average) isomer shift (mm/s); ΔE_Q: quadrupole splitting at the maxima of the distribution (mm/s); $2\epsilon_Q$: (average) quadrupole shift (mm/s); D_δ: linear correlation coefficient between the isomer shift and quadrupole splitting or hyperfine field; D_ϵ: linear correlation coefficient between the quadrupole shift and hyperfine field; Γ: Lorentzian line width (mm/s); P: proportion (%). [b] Fixed parameter. [c] Quadrupole-splitting distribution from 0.00 to 2.00 mm/s. [d] Quadrupole-splitting distribution from 0.20 to 2.00 mm/s. [e] Hyperfine-field distribution from 60 to 560 kOe.

magnetic phases were detected, and all spectra have been recorded on a small velocity scale (±4 mm/s), implying a higher resolution. At lower temperature, however, most spectra showed absorption lines at high velocities, and a higher scale (±11 mm/s) had to be used.

Fe10U1 Oxide Powder. Fe10U1 at RT (Figure 5j) shows broad lines, revealing several Fe^{3+} (super)paramagnetic phases in varying environments. However, no Fe^{2+} phase is detected. The spectrum was first fitted with a quadrupole-splitting distribution where a linear correlation between the isomer shift and quadrupole splitting allowed to refine the fit. Three maxima are resolved in the distribution (Table 2 (RT) and Figure 5k). Considering the parameters deduced from these maxima, a second fit was then attempted with three independent doublets.

TABLE 4: Mössbauer Parameters of Fe10U8 Measured between 14 K and RT[a]

	(super)para Fe^{3+}					magnetic $MgFe_2O_4$-like						
T(K)	δ	ΔE_Q[c]	D_δ	Γ	P	δ	H_{hf}[d]	$2\epsilon_Q$	D_δ	D_ϵ	Γ	P
14	0.40	0.39	0.0194	0.56	14.0	0.39	430	−0.06	−0.0004	−0.0004	0.53	86.0
	0.39	1.03				0.42	509	−0.02				
19	0.41	0.41	0.0267	0.66	25.0	0.42	511	0.01	−0.0001	−0.0001	0.47	75.0
	0.40	1.10										
24	0.41	0.41	0.0253	0.61	46.5	0.42	509	−0.01	−0.0001	−0.0012	0.47	53.5
	0.40	1.05										
30	0.41	0.40	0.0539	0.55	60.0	0.42	506	−0.03	−0.0005	−0.0015	0.52	40.0
	0.39	0.98										
50	0.41	0.40	0.0322	0.54	73.0	0.42	503	−0.03	−0.0010	−0.0007	0.60	27.0
	0.39	0.95										
	0.37	1.50										
80	0.42	0.54	0.0744	0.52	75.0	0.41	491	−0.05	−0.0018	−0.0037	0.53	25.0
	0.39	0.95										
	0.35	1.50										
100	0.40	0.40	0.0311	0.52	79.0	0.42	489	−0.04	−0.0013	−0.0005	0.58	21.0
	0.38	0.95										
	0.37	1.45										
125	0.39	0.40	0.0301	0.52	80.0	0.42	487	−0.06	−0.0011	−0.0005	0.47	20.0
	0.38	0.90										
	0.36	1.40										
150	0.38	0.46	0.0391	0.50	80.0	0.39	479	−0.07	−0.0013	−0.0009	0.61	20.0
	0.37	0.80										
	0.34	1.35										
200	0.36	0.49	0.0481	0.49	81.0	0.35[b]	455	0.01[b]			0.40	19.0
	0.34	0.75										
	0.32	1.35										
250	0.33	0.47	0.0452	0.50	81.5	0.32[b]	423	0.01[b]			0.80	18.5
	0.32	0.75										
	0.29	1.35										
RT	0.32	0.51	0.0687	0.39	100							
	0.29	0.95										
	0.26	1.40										
RT	0.32	0.49	−	0.38	38.5							
bis	0.30	0.86		0.46	45.0							
	0.25	1.27		0.51	16.5							

[a] (Super)para: (super)paramagnetic; H_{hf}: hyperfine field at the maxima of the distribution (kOe); δ: (average) isomer shift (mm/s); ΔE_Q: quadrupole splitting at the maxima of the distribution (mm/s); $2\epsilon_Q$: (average) quadrupole shift (mm/s); D_δ: linear correlation coefficient between the isomer shift and quadrupole splitting or hyperfine field; D_ϵ: linear correlation coefficient between the quadrupole shift and hyperfine field; Γ: Lorentzian line width (mm/s); P: proportion (%). [b] Fixed parameter. [c] Quadrupole-splitting distribution from 0.20 to 2.00 mm/s. [d] Hyperfine-field distribution from 60 to 560 kOe.

The quality of the fit slightly decreases, but more-accurate results are obtained for the Mössbauer parameters and for the proportions of the three phases (Table 2 (RT bis) and Figure 9b). The first doublet can be assigned to Fe^{3+} ions in the O_h sites of MgO or $MgFe_2O_4$ on the basis of the good agreement of its Mössbauer parameters with the values reported by other authors.[34,40] The second doublet has a similar isomer shift, but its quadrupole splitting is larger, suggesting a higher distortion of the O_h sites or nearby structure that is probably due to clustering of the concerned ions. Such a large quadrupole-splitting value is also reported by Bhide and Tambe[38] and by Carles and Rousset[28] for Fe^{3+} ions in the O_h sites of MgO. The third doublet has a smaller isomer shift and a larger quadrupole splitting than the previous ones. It may arise from Fe^{3+} ions in T_d sites of $MgFe_2O_4$ precipitates in MgO, as suggested by Perez et al.[34] and Waychunas.[40] This finding supports the presence of $MgFe_2O_4$-like particles in Fe10U1, as concluded from the XRD results.

The MS at low temperatures reveal that superparamagnetic relaxation takes place below 220 K, where the central part of the spectrum progressively decreases in favor of a broad six-line pattern (Table 2 and Figure 5a, d, and g). At 14 K, the pattern shows an asymmetry typical of a $MgFe_2O_4$-like phase: in particular, the first, second, and third lines are deeper and narrower than the fourth, fifth, and sixth lines (Figure 5a). Indeed, $MgFe_2O_4$ is ferrimagnetic and produces two sextets characteristic of Fe^{3+} in the O_h and T_d sites of the spinel structure.[41] The two sextets have slightly different Mössbauer parameters in the temperature range considered here: $H_{hf}(O_h) - H_{hf}(T_d) = 20$ to 30 kOe, $\delta(O_h) - \delta(T_d) = 0.1$ mm/s, and $2\epsilon_Q(O_h) \approx 2\epsilon_Q(T_d) \approx 0$ mm/s. The asymmetry in the pattern is then due to the different isomer-shift values. However, the size distribution and the varying composition of the $MgFe_2O_4$-like particles in Fe10U1 result in such a broad distribution of the hyperfine field that subcomponents cannot be resolved. De Bakker[42] was confronted with similar patterns obtained for chromium- and zinc-substituted $MgFe_2O_4$. He obtained satisfactory fits with a hyperfine-field distribution including linear correlation between the isomer shift and hyperfine field and between the quadrupole shift and hyperfine field. On the basis of the same procedure, the magnetic part of the present MS was fitted with a hyperfine-field distribution with fields ranging from 60 to 560 kOe, the line ratios being always fixed at 3:2:1 (Figure 5c, f, and i). The linear correlation allowed us to include the asymmetry of the pattern in the fit. When the pattern lines were too weak to produce consistent parameters, no correlation was used, and the isomer-shift and quadrupole-shift values were fixed at expected values. The average Mössbauer parameters obtained at the maximum of the hyperfine-field distribution over the full range of temperature (Table 2) are in good agreement

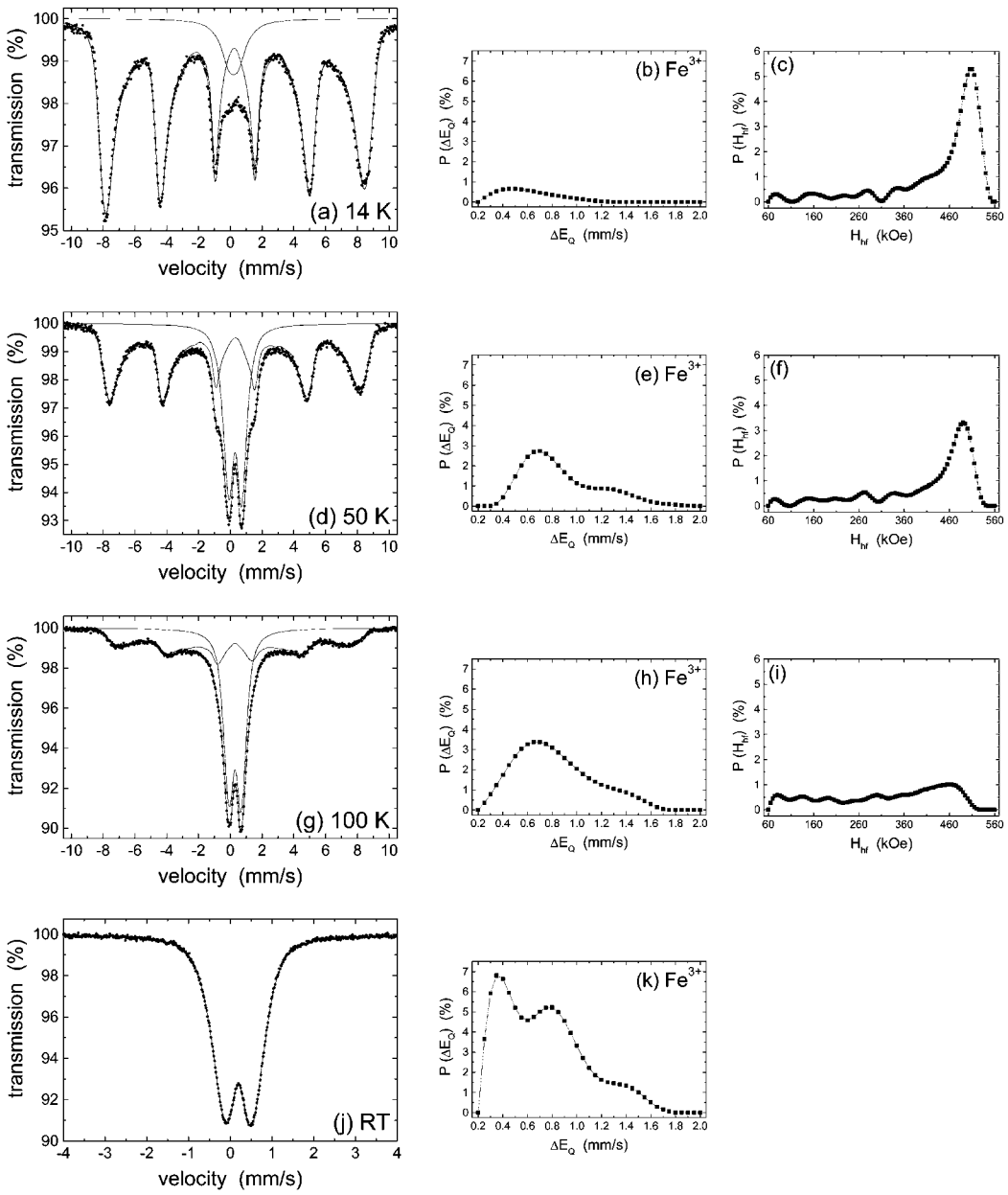

Figure 5. MS of Fe10U1 measured between 14 K and RT (a, d, g, j) and corresponding quadrupole-splitting distributions of the (super)paramagnetic Fe^{3+} phases (b, e, h, k) and hyperfine-field distributions of the magnetic $MgFe_2O_4$-like phase (c, f, i).

with those expected for $MgFe_2O_4$-like particles undergoing superparamagnetic relaxation.[42] We acknowledge that this fitting procedure is unrealistic, notably because of the non-null value of the quadrupole shift, but it is nevertheless an adequate fitting model that allows us to compare different samples.

Regarding the (super)paramagnetic Fe^{3+} phases at low temperatures, they were fitted with the same quadrupole-splitting distribution as used at RT, giving rise to consistent parameter values. Figure 8 shows the regular decrease of the (super)-paramagnetic Fe^{3+} proportion in Fe10U1 with decreasing temperature in favor of the magnetic phase. From 125 K downward, the third maximum in the distribution does not appear anymore (Table 2 and Figure 5e and h). Moreover, the proportion of the second maximum decreases faster than the proportion of the first one, which appears alone in the distribution at 14 K (Table 2 and Figure 5b). The third maximum was attributed to Fe^{3+} ions in T_d sites of $MgFe_2O_4$ and reflects the presence of large Fe^{3+} clusters. It is therefore consistent that these clusters are the first to split magnetically with decreasing temperature. The second maximum was attributed to Fe^{3+} ions in distorted O_h sites. The magnetic splitting at low temperature indeed suggests that these ions form small superparamagnetic clusters. The proportion of Fe^{3+} that remains at 14 K is essentially characteristic of isolated paramagnetic Fe^{3+} ions substituted in the MgO lattice.

Fe10U4 Oxide Powder. The same fitting procedures were considered for the MS of this sample (Table 3 and Figure 6). At RT, the Fe^{3+} quadrupole-splitting distribution exhibits two maxima (Table 3 (RT) and Figure 6i and k), and a proper fit could also be obtained with two independent doublets (Table 3 (RT bis) and Figure 9d). These two components were attributed to Fe^{3+} in the O_h sites of MgO (or possibly of $MgFe_2O_4$ for the first one), the larger quadrupole splitting of the second one suggesting distorted sites due to Fe^{3+} clustering and thus potential $MgFe_2O_4$-like particles. However, no T_d Fe^{3+} was detected. Moreover, a second quadrupole-splitting distribution had to be used to fit the spectrum properly (Figure 6i and j). This extra pattern is typical of Fe^{2+} ions, as revealed by its isomer-shift value (Table 3). Two maxima were detected in the distribution (Figure 6j).

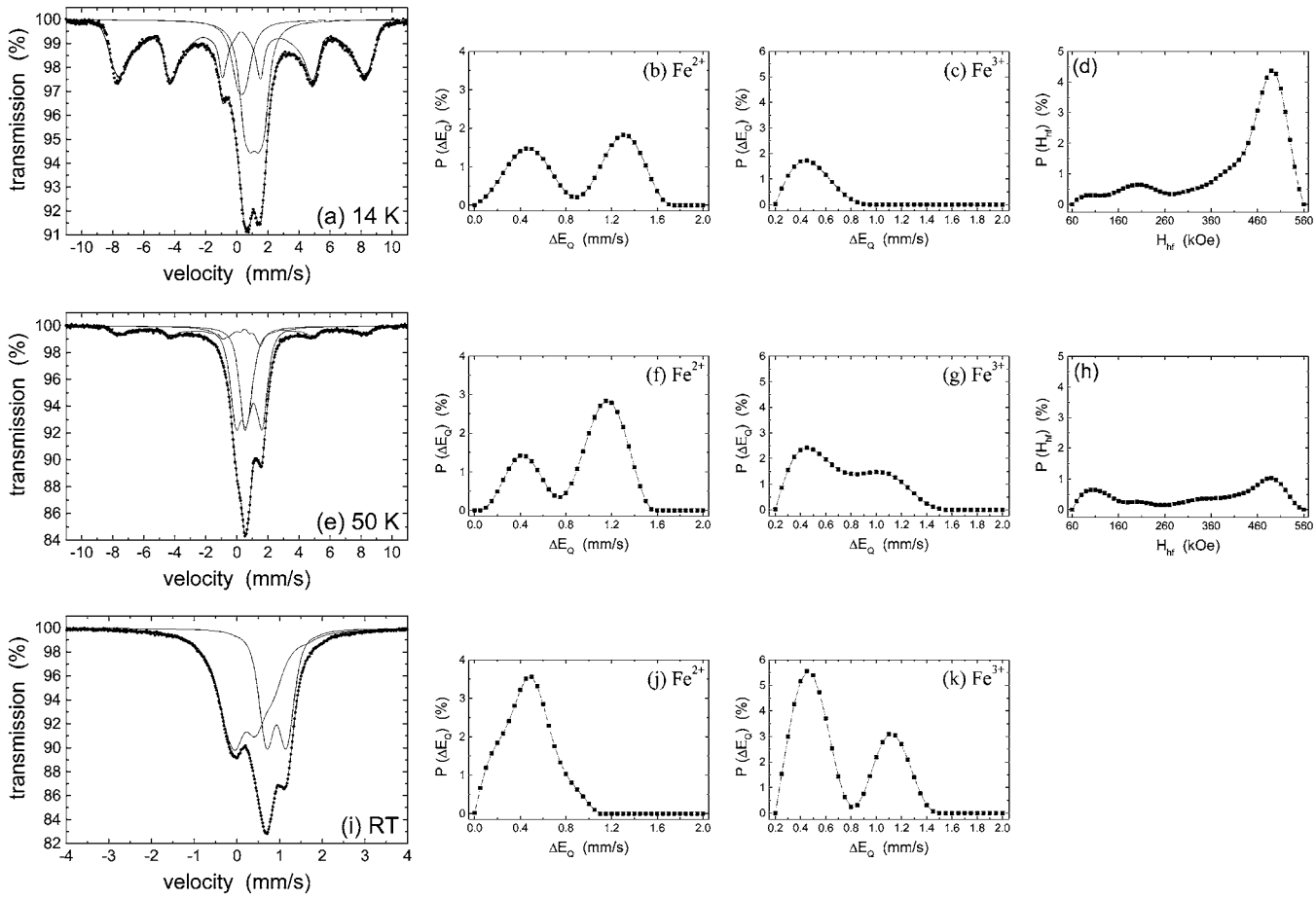

Figure 6. MS of Fe10U4 measured between 14 K and RT (a, e, i) and corresponding quadrupole-splitting distributions of the (super)paramagnetic Fe^{2+} phases (b, f, j) and (super)paramagnetic Fe^{3+} phases (c, g, k) and hyperfine-field distributions of the magnetic $MgFe_2O_4$-like phase (d, h).

Upon decreasing the temperature, the Fe^{3+} phases progressively split into a magnetic pattern comparable to the one described above (Figure 6a, d, e, and h). Figure 8 shows the (super)paramagnetic Fe^{3+} proportion versus the measuring temperature, with values normalized to 100% at RT. The decrease of the (super)paramagnetic Fe^{3+} proportion starts at 200 K and shows a more gentle slope than for Fe10U1. Magnetic splitting at lower temperatures suggests smaller Fe^{3+} clusters in Fe10U4 compared to those in Fe10U1, which is compatible with the apparent absence of T_d Fe^{3+}. At 14 K, the second maximum of the Fe^{3+} quadrupole-splitting distribution has completely disappeared, revealing the proportion of isolated paramagnetic Fe^{3+} ions substituted in the MgO lattice (Table 3 and Figure 6c). This proportion is comparatively higher in Fe10U4 than in Fe10U1, as shown in Figure 8.

The two maxima of the Fe^{2+} quadrupole-splitting distribution are increasingly more separated with decreasing temperature, the second one showing a drastic increase in quadrupole splitting on lowering the temperature (Table 3 and Figure 6b, f, and j). The quadrupole splitting of Fe^{2+} ions in crystalline fields of low symmetry is very sensitive to temperature variations, and by referring to other work,[28,31,33−36] these two maxima can be attributed to Fe^{2+} ions distributed in the O_h sites of MgO, the one with larger quadrupole splitting revealing Fe^{2+} ions, which form clusters. Moreover, the Fe^{2+} proportion can be considered to be constant down to $T = 30$ K, but it decreases significantly at 14 K (Table 3), which is accompanied by a decrease in the second maximum in the Fe^{2+} quadrupole-splitting distribution (Figure 6b). This finding suggests that the Fe^{2+} clusters can be considered to be very small superparamagnetic particles, as reported by other authors.[33,35] Consequently, the hyperfine-field distribution at 14 K (Figure 6d) includes the contribution of the Fe^{2+} clusters, which have become magnetic at that low temperature.

Fe10U8 Oxide Powder. The Fe10U8 MS at RT was fitted with a quadrupole-splitting distribution characteristic of Fe^{3+} phases (Table 4 (RT) and Figure 7j and k). Using a linear correlation between the isomer shift and quadrupole splitting, three maxima are detected in the distribution profile (Figure 7k). An adequate fit was also obtained with three independent doublets (Table 4 (RT bis) and Figure 9f), giving more-accurate information on these three phases that can be attributed, as in the case of Fe10U1, to O_h Fe^{3+} ions in MgO or $MgFe_2O_4$, O_h Fe^{3+} ions that form clusters in MgO, and T_d Fe^{3+} ions revealing the presence of $MgFe_2O_4$-like particles. No Fe^{2+} phase is detected.

At low temperature, superparamagnetic relaxation takes place as in the two previous specimens, and a similar magnetic pattern appears (Figure 7a, c, d, f, g, and i). However, the evolution of the (super)paramagnetic Fe^{3+} proportion with decreasing temperature is different from that obtained for Fe10U1 and Fe10U4 (Figure 8). Indeed, the (super)paramagnetic Fe^{3+} proportion in Fe10U8 decreases rapidly below RT to reach a constant value of about 80%, which further remains constant between 250 and 100 K. It subsequently slightly decreases between 100 and 50 K and then steeply decreases below 50 K. Moreover, below 50 K, the third maximum in the Fe^{3+} quadrupole-splitting distribution disappears (Figure 7b and e). This suggests a bimodal size distribution of Fe^{3+} clusters that is considerably more established than in Fe10U1. The magnetic splitting slightly below RT

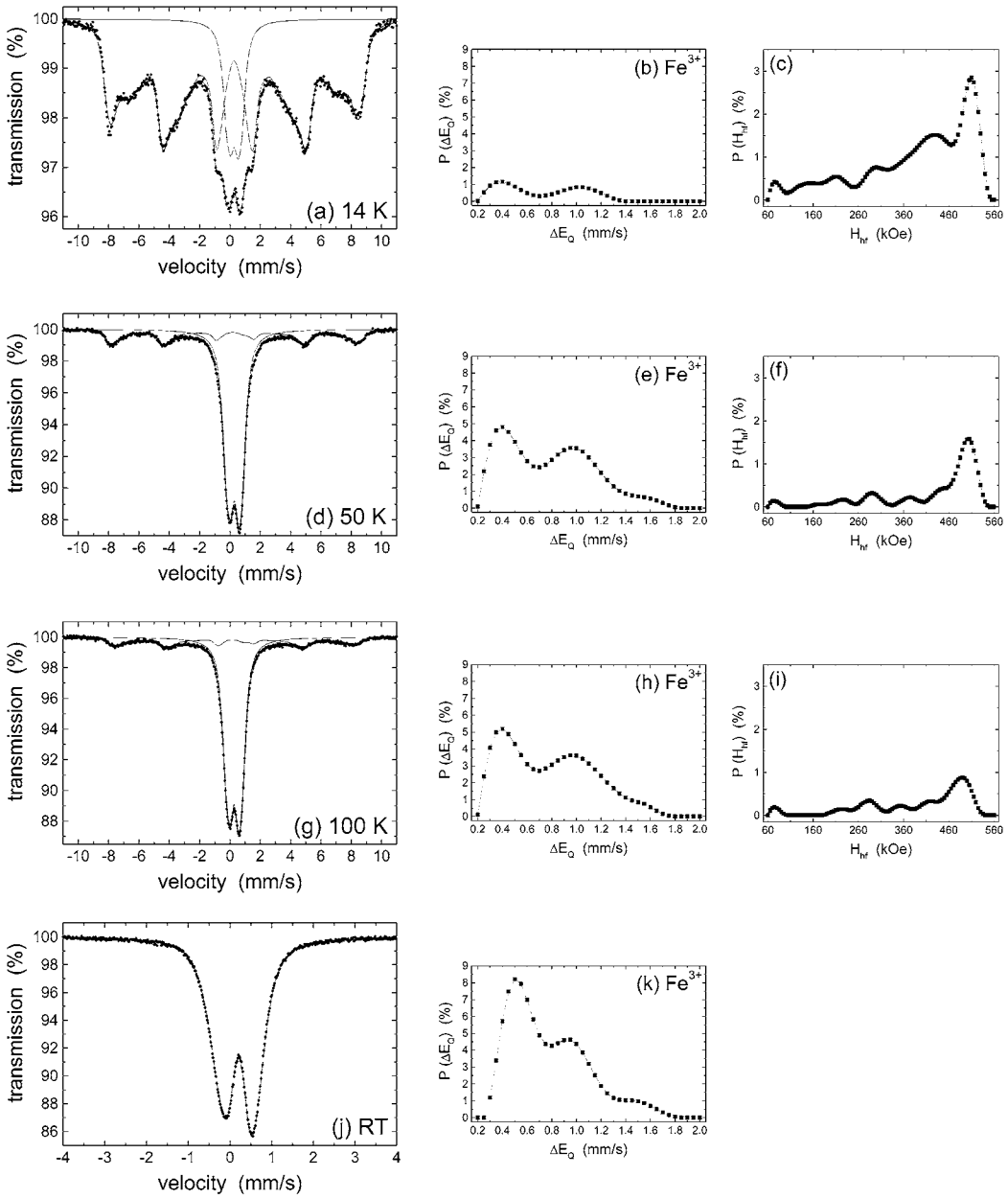

Figure 7. MS of Fe10U8 measured between 14 K and RT (a, d, g, j) and corresponding quadrupole-splitting distributions of the (super)paramagnetic Fe^{3+} phases (b, e, h, k) and hyperfine-field distributions of the magnetic $MgFe_2O_4$-like phase (c, f, i).

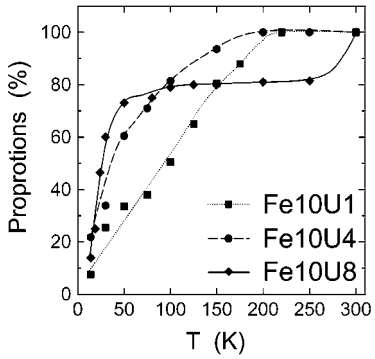

Figure 8. (Super)paramagnetic Fe^{3+} proportions in Fe10U1, Fe10U4, and Fe10U8 as determined from the Mössbauer study (values from Tables 2, 3, and 4, respectively) versus the measuring temperature. The values for Fe10U4 were normalized to 100% at RT for the sake of comparison. The lines are guides for the eye.

reveals $MgFe_2O_4$-like particles that are larger than those detected in Fe10U1, confirming the qualitative result of the XRD analysis (Figure 2). The decrease at temperatures below 50 K, however, suggests very small Fe^{3+} clusters in MgO that are probably not detected in the XRD analysis. At 14 K, the second maximum at $\Delta E_Q \approx 1.00$ mm/s is still present in the Fe^{3+} quadrupole-splitting distribution of Fe10U8 (Figure 7b), which was not the case for Fe10U1 and Fe10U4. Moreover, a second maximum at lower field ($H_{hf} \approx 430$ kOe) is clearly observed in the hyperfine-field distribution at 14 K (Table 4 and Figure 7c), denoting the superparamagnetic relaxation of these very small clusters.

Comparison of Fe5 and Fe10 Oxide Powders. Table 5 gives the RT Mössbauer parameters of Fe5U1, Fe5U4, and Fe5U8 together with the corresponding parameters for Fe10U1, Fe10U4, and Fe10U8 discussed in the previous sections. Three independent Fe^{3+} doublets and one Fe^{2+} quadrupole-splitting distribution were considered for the fitting of the MS that are presented in Figure 9.

Fe5U1 contains no Fe^{2+} phase, and the Mössbauer parameters of the three Fe^{3+} doublets are similar to those of Fe10U1. The

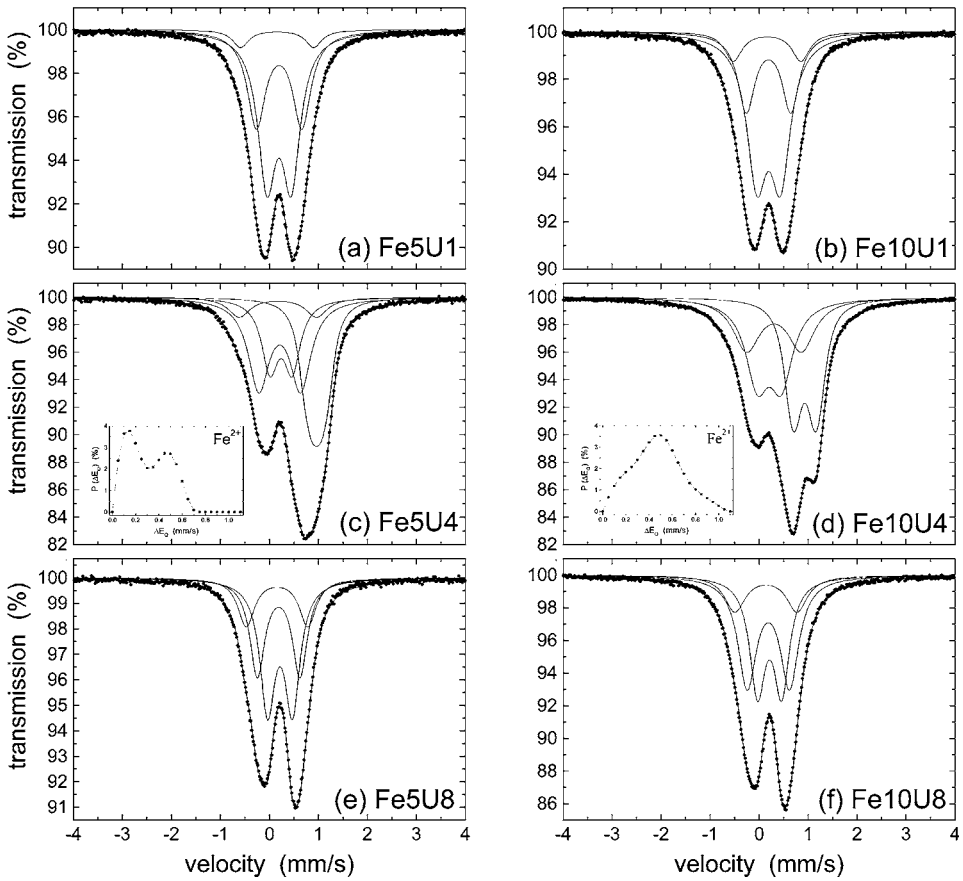

Figure 9. MS of Fe5U1 (a) and Fe10U1 (b), Fe5U4 (c) and Fe10U4 (d), and Fe5U8 (e) and Fe10U8 (f) measured at RT. Three independent doublets were considered to characterize the Fe^{3+} phases.

TABLE 5: Mössbauer Parameters of Fe5U1 and Fe10U1, Fe5U4 and Fe10U4, and Fe5U8 and Fe10U8 Measured at RT[a]

	O_h Fe^{2+}				O_h Fe^{3+} [b]				O_h Fe^{3+} [c]				T_d Fe^{3+}			
oxide powder	δ	ΔE_Q[d]	Γ	P	δ	ΔE_Q	Γ	P	δ	ΔE_Q	Γ	P	δ	ΔE_Q	Γ	P
Fe**5**U**1**					0.30	0.50	0.45	56.5	0.30	0.93	0.45	37.5	0.26	1.49	0.40	6.0
Fe**10**U**1**					0.30	0.49	0.50	60.0	0.30	0.91	0.43	29.0	0.27	1.38	0.43	11.0
Fe5U**4**	1.07	0.13 0.45	0.29	32.0	0.35	0.45	0.41	22.5	0.32	0.85	0.52	37.0	0.28	1.58	0.54	8.5
Fe**10**U**4**	1.04	0.20 0.48	0.34	37.0	0.32	0.49	0.57	36.0	0.41	1.12	0.67	27.0				
Fe**5**U**8**					0.32	0.51	0.37	46.0	0.29	0.87	0.37	34.5	0.26	1.26	0.41	19.5
Fe**10**U**8**					0.32	0.49	0.38	38.5	0.30	0.86	0.46	45.0	0.25	1.27	0.51	16.5

[a] Three independent doublets were considered to characterize the Fe^{3+} phases. O_h: octahedral sites; T_d: tetrahedral sites; δ: (average) isomer shift (mm/s); ΔE_Q: quadrupole splitting (at the maxima of the distribution) (mm/s); Γ: Lorentzian line width (mm/s); P: proportion (%) [b] Isolated ions in MgO (or possibly ions in $MgFe_2O_4$). [c] Ions forming clusters in MgO. [d] Quadrupole-splitting distribution from 0.00 to 1.10 mm/s.

relatively small variations in the proportions are not significant enough to infer differences between the two samples.

Fe5U4 exhibits an Fe^{2+} quadrupole-splitting distribution with two clearly separated maxima (Figure 9c). The global Fe^{2+} proportion in Fe5U4 is slightly smaller than the one in Fe10U4 (Table 5), revealing that the number of substituted Fe^{2+} ions is more than twice as large in Fe10U4 as in Fe5U4. However, contrary to the proportion in Fe10U4, the proportion of the first maximum in the Fe^{2+} quadrupole-splitting distribution of Fe5U4 is higher than the proportion of the second one (Figure 9c and d), showing that the larger number of Fe^{2+} ions substituted in the MgO lattice of Fe10U4 favors the formation of Fe^{2+} clusters. Moreover, the proportion of O_h Fe^{3+} ions that form clusters is higher in Fe5U4 than in Fe10U4, and the MS of Fe5U4 contains a doublet characteristic of T_d Fe^{3+}, which is not detected in Fe10U4. This reveals a higher degree of Fe^{3+} clustering in Fe5U4, which favors the formation of $MgFe_2O_4$-like particles. This can be associated with the slightly higher S_{ss} value measured for Fe5U4 than for Fe10U4, suggesting smaller particles on the surface of the MgO grains for Fe5U4 (Table 1). It thus appears that the substitution of Fe^{2+} and Fe^{3+} ions in the MgO lattice is considerably favored using 10 cat. % iron rather than 5 cat. % iron when a urea ratio of 4 is used for the combustion.

The results for Fe5U8 are similar to those obtained for Fe10U8, in particular, showing a rather large proportion of T_d Fe^{3+} ions. It can thus be extrapolated that a similar bimodal size distribution, corresponding to large $MgFe_2O_4$-like particles and small Fe^{3+} clusters, respectively, is also the case for this sample.

As suggested above, the greenish color observed for the powders synthesized with a urea ratio of 4 points to the presence

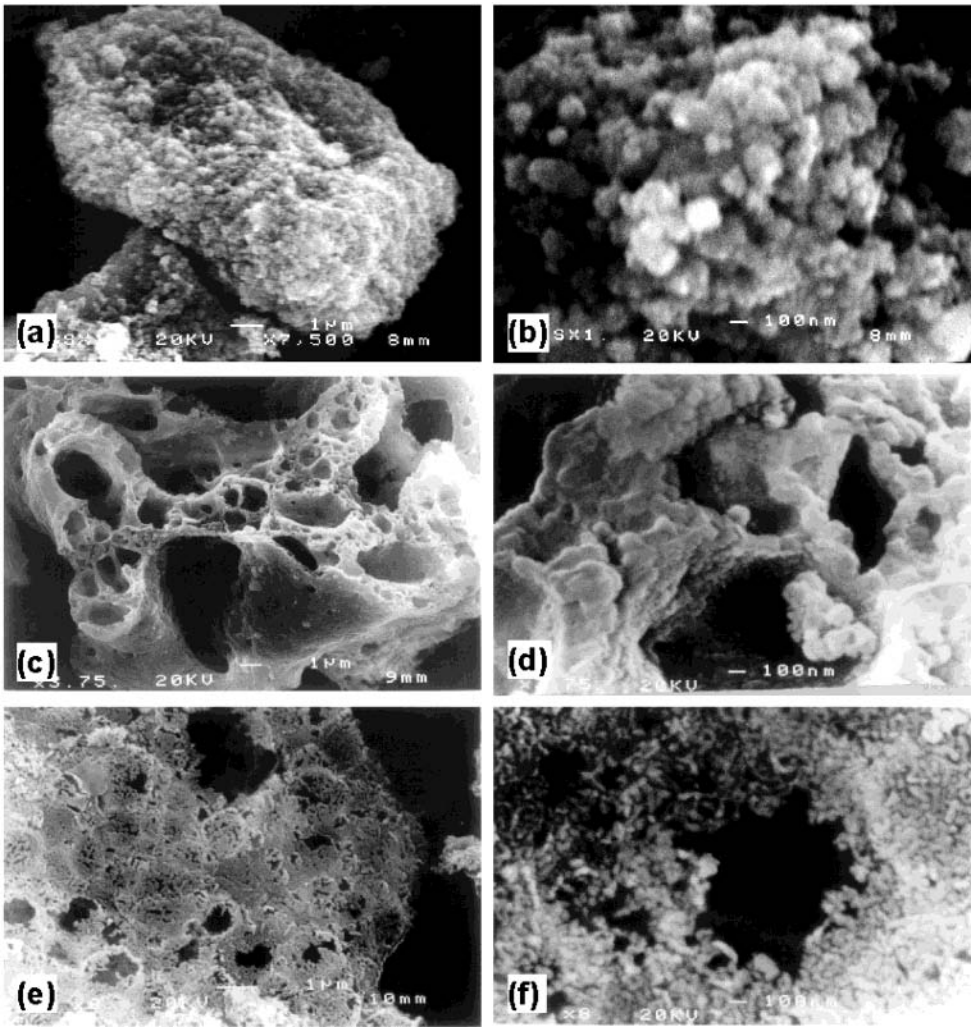

Figure 10. SEM images of Fe10U1 (a, b), Fe10U4 (c, d), and Fe10U8 (e, f).

of Fe^{2+} ions. For powders prepared with ratios of 1 and 8, no Fe^{2+} is detected, and the Fe^{3+} ions are responsible for the red color of the powders. Moreover, the green and red areas observed in the FeU4 oxide powders prepared per batch of 6 g were analyzed separately by Mössbauer spectroscopy. The green area is characterized by a high proportion of Fe^{2+} ions (50% of all the iron) and by Fe^{3+} ions that are well dispersed in the O_h sites of MgO (20%), whereas the red area is characterized by a high proportion of T_d Fe^{3+} ions (35%) and by O_h Fe^{3+} ions, which form clusters in MgO (55%). Even if the present FeU4 oxide powders prepared per batch of 2 g appear to be homogeneous because of a better expansion of the powder during the combustion process, a local agglomeration of Fe^{3+} clusters can be expected.

Scanning Electron Microscopy. SEM images (Figure 10) show the microstructural differences between Fe10U1, Fe10U4, and Fe10U8. For Fe10U1, grains on the order of 10 μm are observed (Figure 10a). At a higher magnification, it appears that these grains consist of closely packed primary grains on the order of 100 nm (Figure 10b). For Fe10U4, no such individual grains can be observed, but the combustion product appears to be a porous foam, showing large open cavities (Figure 10c). At higher magnification, however, it appears that this foam also consists of closely packed primary grains, the size of which seems to be slightly larger than in Fe10U1 (Figure 10d). For Fe10U8, the product is even more porous (Figure 10e), and the primary grains are very loosely packed. Moreover, the primary grain size is smaller than in Fe10U4 and Fe10U1. Note that the primary grain sizes evaluated on these images seem to be globally larger than the crystallite sizes obtained from the widths at half-maximum of the MgO peaks in the XRD patterns (Figure 4), showing that not all of the primary grains are monocrystalline. $MgFe_2O_4$-like particles could not be detected in the SEM images.

These observations can be correlated to the evolution of S_{ss} versus the urea ratio presented in Figure 1. For Fe10U1, S_{ss} is mainly influenced by the small $MgFe_2O_4$-like particles detected by XRD and Mössbauer spectroscopy. Indeed, an increase of the iron content in the oxide corresponds to an increase of S_{ss} (Table 1), whereas the microstructure remains compact (Figure 10a and b). When the urea ratio increases from 1 to 4, the temperature during the reaction increases, favoring sintering of the material and coalescence of the crystallites. Moreover, the XRD and Mössbauer spectroscopy analyses have shown that more iron is dissolved in the MgO lattice. This explains the decrease of S_{ss} observed between the urea ratios of 1 and 4 (Figure 1). The increase of the gas release explains the porosity of the foam observed for Fe10U4 (Figure 10c and d), but the pores are too large to increase the S_{ss} values notably. When the urea ratio increases from 4 to 8, the temperature of the reaction decreases, leading to very little sintering and thus to much smaller primary grains and crystallites. Moreover, the gas release and the resulting expansion of the material considerably increase, giving rise to the more porous foam observed for Fe10U8 (Figure 10e and f). Consequently, the maximal S_{ss} value is observed for Fe10U8. Indeed, the $MgFe_2O_4$-like particles

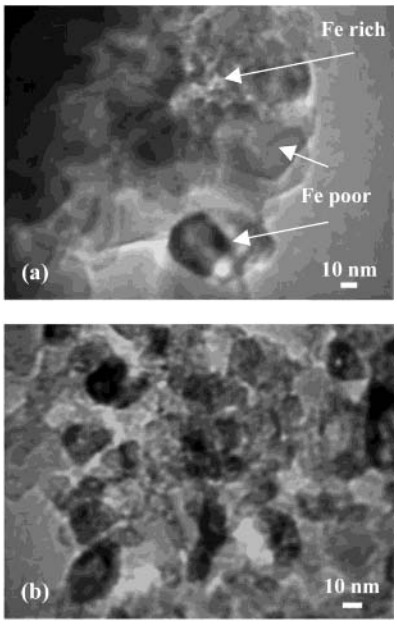

Figure 11. TEM images of Fe10U1 (a) and Fe10U8 (b).

detected by XRD and Mössbauer spectroscopy make a negligible contribution to S_{ss}, as reflected by the weak increase of S_{ss} with the iron content (Table 1).

Transmission Electron Microscopy. In the FeU1 and FeU8 oxides, a high proportion of iron forms Fe^{3+} clusters and $MgFe_2O_4$-like particles. To get more information about the repartition of iron outside the MgO lattice in these samples, Fe10U1 and Fe10U8 were examined by TEM. Many EDX measurements were carried out on different areas of the samples. The impact position and the surface area of the beam were always adjusted to be characteristic of the surface of the studied area. Magnesium and iron proportions (atom %) were compared.

Figure 11 shows typical TEM images of Fe10U1 and Fe10U8. For Fe10U1, unstructured areas are observed among cubic forms. The cubic forms are typical of the rock salt structure of MgO crystallites. They contain very little iron (1−2 at %). However, the unstructured areas are very rich in iron (40−50 atom %), revealing a large amount of agglomeration of the iron in Fe10U1. For Fe10U8, no such difference could be observed, and all measurements gave an iron proportion of 5 to 15 atom %, revealing that iron is much more dispersed in Fe10U8 than in Fe10U1.

Conclusions

We attempted to synthesize $Mg_{1-x}Fe_xO$ oxide solid solutions by the combustion route with the aim of studying the influences of the nitrate/urea ratio and the iron content on the valency and distribution of the iron ions and phases. The Fe/MgO oxides synthesized with the so-called stoichiometric ratio contain large grains (∼10 μm) that consist of highly agglomerated small primary grains (∼35 nm), some of them being made up of several crystallites. No Fe^{2+} ions substitute for Mg^{2+} in the MgO lattice, and most of the Fe^{3+} ions form clusters and $MgFe_2O_4$-like particles that are poorly dispersed in the powder, as revealed by large fluctuations of the local iron content. The combustion conditions are therefore not sufficiently reducing. To increase the substitution ratio of the iron cations in the MgO lattice, the urea proportion was gradually increased up to a factor 8. Increasing it by a factor in the range of 3.5−4.5 leads to combustion conditions that would correspond as closely as possible to the stoichiometric region as defined by Zhang and Stangle.[19] Indeed, the so-obtained oxides contain about 40% of the total iron substituting as Fe^{2+} in MgO, and a large proportion of the Fe^{3+} ions are dispersed in the O_h sites of MgO. However, local agglomeration of Fe^{3+} clusters can be expected in these samples. The powders appear as a foam with large cavities, resulting from the sintering of small primary grains (∼60 nm). For a urea ratio increased by a factor of 8, the considerable expansion due to the gas release during the combustion results in a very porous powder constituted of small loosely packed MgO primary grains (∼25 nm). No Fe^{2+} ions are formed, and the Fe^{3+} ions are present in iron agglomerates with a bimodal size distribution: very small Fe^{3+} clusters that are not detected for other urea ratios and $MgFe_2O_4$-like particles that are larger, but much better dispersed, than those detected for a urea ratio of 1. The Fe/MgO oxides prepared with urea ratios of 1, 4, and 8 are clearly different from one another, presenting several well-defined iron species. The formation of CNTs from these powders (with different iron contents) upon reduction in a H_2/CH_4 gas atmosphere is studied in a companion paper.[21]

Acknowledgment. We thank Mr. L. Datas for his assistance with the TEM observations, which have been performed at the Service Commun de Microscopie Electronique à Transmission—Université Paul-Sabatier. This research is supported by the Belgian National Program of Inter-University Attraction Pole on Reduced Dimensionality Systems (P4/10), by the Fund for Scientific Research—Flanders, and by the Franco-Belgian TOURNESOL program (T99/006-T99/045).

References and Notes

(1) Hafner, J. H.; Bronikowski, M. J.; Azamian, B. K.; Nikolaev, P.; Rinzler, A. G.; Colbert, D. T.; Smith, K. A.; Smalley, R. E. *Chem. Phys. Lett.* **1998**, *296*, 195.

(2) Flahaut, E.; Peigney, A.; Laurent, Ch.; Rousset, A. *J. Mater. Chem.* **2000**, *10*, 249.

(3) Bacsa, R. R.; Laurent, Ch.; Peigney, A.; Bacsa, W. S.; Vaugien, Th.; Rousset, A. *Chem. Phys. Lett.* **2000**, *323*, 566.

(4) Peigney, A.; Coquay, P.; Flahaut, E.; Vandenberghe, R. E.; De Grave, E.; Laurent, Ch. *J. Phys. Chem. B* **2001**, *105*, 9699.

(5) Herrera, J. E.; Balzano, L.; Borgna, A.; Alvarez, W. E.; Resasco, D. E. *J. Catal.* **2001**, *204*, 129.

(6) Alvarez, W. E.; Kitiyanan, B.; Borgna, A.; Resasco, D. E. *Carbon* **2001**, *39*, 547.

(7) Li, Y.; Liu, J.; Wang, Y.; Wang, Z. L. *Chem. Mater.* **2001,** *13*, 1008.

(8) Peigney, A.; Laurent, Ch.; Dobigeon, F.; Rousset, A. *J. Mater. Res.* **1997**, *12*, 613.

(9) Peigney, A.; Laurent, Ch.; Dumortier, O.; Rousset, A. *J. Eur. Ceram. Soc.* **1998**, *18*, 1995.

(10) Laurent, Ch.; Peigney, A.; Rousset, A. *J. Mater. Chem.* **1998**, *8*, 1263.

(11) Laurent, Ch.; Peigney, A.; Flahaut, E.; Rousset, A. *Mater. Res. Bull.* **2000**, *35*, 661.

(12) Govindaraj, A.; Flahaut, E.; Laurent, Ch.; Peigney, A.; Rousset, A.; Rao, C. N. R. *J. Mater. Res.* **1999**, *14*, 2567.

(13) Coquay, P.; De Grave, E.; Vandenberghe, R. E.; Dauwe, C.; Flahaut, E.; Laurent, Ch.; Peigney, A.; Rousset, A. *Acta Mater.* **2000**, *48*, 3015.

(14) Quénard, O.; De Grave, E.; Laurent, Ch.; Rousset, A. *J. Mater. Chem.* **1997**, *7*, 2457.

(15) Flahaut, E.; Govindaraj, A.; Peigney, A.; Laurent, Ch.; Rousset, A.; Rao, C. N. R. *Chem. Phys. Lett.* **1999**, *300*, 236.

(16) Kingsley, J. J.; Patil, K. C. *Mater. Lett.* **1988**, *6*, 427.

(17) Patil, K. C. *Bull. Mater. Sci.* **1993**, *16*, 533.

(18) Jain, S. R.; Adiga, K. C.; Pai Verneker, V. R. *Combust. Flame* **1981**, *40*, 71.

(19) Zhang, Y.; Stangle, G. C. *J. Mater. Res.* **1994**, *9*, 1997.

(20) Bacsa, R. R.; Laurent, Ch.; Peigney, A.; Vaugien, Th.; Flahaut, E.; Bacsa, W. S.; Rousset, A. *J. Am. Ceram. Soc.* **2002**, *85*, 2666.

(21) Coquay, P.; Peigney, A.; De Grave, E.; Vandenberghe, R. E.; Laurent, Ch. *J. Phys. Chem. B* **2002**, *106*, 13199.

(22) Dinnebier, R. E.; Eysel, W. Abstract of Powder Diffraction Satellite Meeting of the XVth Congress of the International Union of Crystallography, Toulouse, France, 1990; p 279.

(23) Holland, T. J. B.; Redfern, S. A. T. *Mineral. Mag.* **1997**, *61*, 65.

(24) Vandenberghe, R. E.; De Grave, E.; de Bakker, P. M. A. *Hyperfine Interact.* **1994**, *83*, 29.
(25) Berthet, A. Ph.D. Thesis, University of Nancy, Nancy, France, 1963.
(26) Berthet, A.; Perrot, P. *Mem. Sci. Rev. Metall.* **1970**, *LXVII*, 747.
(27) Trinel-Dufour, M. C.; Perrot, P. *Ann. Chim.* **1977**, *2*, 309.
(28) Carles, V.; Rousset, A. *Solid State Ionics* **1996**, *83*, 309.
(29) Blank, S. L.; Pask, J. A. *J. Am. Ceram. Soc.* **1969**, *52*, 669.
(30) Brynestad, J.; Flood, H. *Z. Elektrochem.* **1958**, *62*, 953.
(31) Boudart, M.; Delbouille, A.; Dumesic, J. A.; Khammouma, S.; Topsoe, H. *J. Catal.* **1975**, *37*, 486.
(32) Yamaguchi, G.; Tokuda, T. *J. Ceram. Assoc. Jpn.* **1968**, *76*, 350.
(33) Jing, J.; Campbell, S. J. *Hyperfine Interact.* **1991**, *68*, 283.
(34) Perez, A.; Marest, G.; Sawicka, B. D.; Sawicki, J. A.; Tyliszczak, T. *Phys. Rev. B* **1983**, *28*, 1227.
(35) Simkin, D. J.; Ficalora, P. J.; Bernheim, R. A. *Phys. Lett.* **1965**, *19*, 536.
(36) Topsoe, H.; Dumesic, J. A.; Derouane, E. G.; Clausen, B. S.; Morup, S.; Villadsen, J.; Topsoe, N. *Stud. Surf. Sci. Catal.* **1979**, *3*, 365.
(37) Woods, K. N.; Fine, M. E. *J. Appl. Phys.* **1969**, *40*, 3425.
(38) Bhide, V. G.; Tambe, B. R. *J. Mater. Sci.* **1969**, *4*, 955.
(39) Krawitz, A.; Cohen, J. B. *J. Am. Ceram. Soc.* **1974**, *57*, 186.
(40) Waychunas, G. A. *J. Mater. Sci.* **1983**, *18*, 195.
(41) De Grave, E.; Govaert, A.; Chambaere, D.; Robbrecht, G. *Physica B* **1979**, *96*, 103.
(42) De Bakker, P. Ph.D. Thesis, University of Ghent, Ghent, Belgium, 1994.